X-ray propagation microscopy of biological cells using waveguides as a quasipoint source

K. Giewekemeyer,[1] S. P. Krüger,[1] S. Kalbfleisch,[1] M. Bartels,[1] C. Beta,[2,3] and T. Salditt[1]
[1]*Institut für Röntgenphysik, Georg-August-Universität Göttingen, 37077 D-Göttingen, Germany*
[2]*Institut für Physik und Astronomie, Universität Potsdam, 14476 Potsdam/Golm, D-Germany*
[3]*Max-Planck-Institut für Dynamik und Selbstorganisation, 37077 D-Göttingen, Germany*
(Received 16 April 2010; published 7 February 2011)

We have used x-ray waveguides as highly confining optical elements for nanoscale imaging of unstained biological cells using the simple geometry of in-line holography. The well-known twin-image problem is effectively circumvented by a simple and fast iterative reconstruction. The algorithm which combines elements of the classical Gerchberg-Saxton scheme and the hybrid-input-output algorithm is optimized for phase-contrast samples, well-justified for imaging of cells at multi-keV photon energies. The experimental scheme allows for a quantitative phase reconstruction from a single holographic image without detailed knowledge of the complex illumination function incident on the sample, as demonstrated for freeze-dried cells of the eukaryotic amoeba *Dictyostelium discoideum*. The accessible resolution range is explored by simulations, indicating that resolutions on the order of 20 nm are within reach applying illumination times on the order of minutes at present synchrotron sources.

DOI: 10.1103/PhysRevA.83.023804 PACS number(s): 42.30.Rx, 07.85.Tt, 87.80.−y

I. INTRODUCTION

Holographic projection imaging with multi-keV x-ray radiation in combination with tomographic reconstruction has a unique potential for lensless three-dimensional image reconstruction [1–4], bringing together the earlier concepts of geometric magnification [5] by a divergent beam and the principle of in-line holography [6]. The sample can be reconstructed as in reference-beam holography [7] by a direct (single-step) backpropagation. However, the image quality is severely limited by the well-known twin image problem of (in-line) holography. Experimental remedies used in the past include the recording of multiple holograms at various detector-to-sample positions [2,3], or a complete knowledge of the illumination function [8], both followed by iterative phase retrieval.

Here we show that the quasispherical wave front exiting from a two-dimensional x-ray waveguide (WG) [9,10] can be used advantageously for holographic image recording from an unstained biological cell, extended by a robust and quickly converging iterative reconstruction scheme applied to a single holographic image. The very high beam confinement substantially below 20 nm, which is possible using new-generation x-ray WGs [11–13], leads to stable reconstructions for weakly scattering biological objects without complete knowledge of the complex valued illumination function, even in the presence of intensity fluctuations. The method is well-adapted for the experimental situation of an essentially pure phase-contrast specimen, and takes photon noise effects into account quantitatively.

Compared to coherent diffractive imaging (CDI) with plane waves [14–16], holographic recording is not *a priori* limited to samples of finite support and enables a significantly faster object reconstruction, compared to the slow convergence of many iterative reconstruction algorithms. If, in addition, some empty beam regions are present around the sample, we find that remaining artifacts due to well-known zeros in the contrast transfer function (CTF) of free-space propagation in the Fresnel regime [17] can be almost fully suppressed. As we show below, this leads to phase reconstructions with low and quantifiable errors. Moreover, using quasispherical wave fronts exiting the WG, the detector pixels can be filled much more evenly than for plane wave illumination, avoiding complications associated with a high dynamic range of the signal, in particular pixel saturation and loss of information due to beam stops. Finally, by holographic interference, a weak scattering amplitude can be amplified high above background signals of residual scatter, dark current, or readout noise.

II. EXPERIMENTAL DETAILS

The experiment (for a schematic of the setup, see Fig. 1) was performed at the ID22-NI undulator beamline of the European Synchrotron Radiation Facility (Grenoble, France). Pink-beam undulator radiation with a photon energy of 17.5 keV ($\Delta E/E \simeq 0.02$) was focused horizontally and vertically by two Kirkpatrick-Baez (KB) mirrors down to lateral dimensions of $D_{\mathrm{horz}} = 129$ nm full width at half maximum (FWHM) and $D_{\mathrm{vert}} = 166$ nm. The WG system, placed into the focus of the KB mirrors, consisted of two planar high-transmission, one-dimensionally confining WG structures [11], glued onto each other in a crossed geometry (see Fig. 1). The autocorrelation FWHM, calculated from the empty WG far field, was below 20 nm along all directions [13]. Thus, the illumination of the sample can be interpreted as that of an effective source with a lateral extension well below the WG guiding core dimension (35 nm in both directions).

Freeze-dried cells of the eukaryotic amoeba *Dictyostelium discoideum* were placed on a thin polyimide film at a distance $z_1 = 8.83$ mm from the WG exit plane, as determined with an on-axis optical video microscope (see Fig. 1). Before the experiment, the cells of the *D. discoideum* wild-type strain AX2-214 were allowed to adhere onto a thin polyimide film (Mitegen, USA) before rapid freezing in liquid ethane to prevent crystallization of the phosphate buffer solution (2 g/L KH_2PO_4, 0.36 g/L $Na_2HPO_4 \cdot 2H_2O$, pH 6.0). Afterwards, the cells were freeze-dried in a commercial freeze-drier

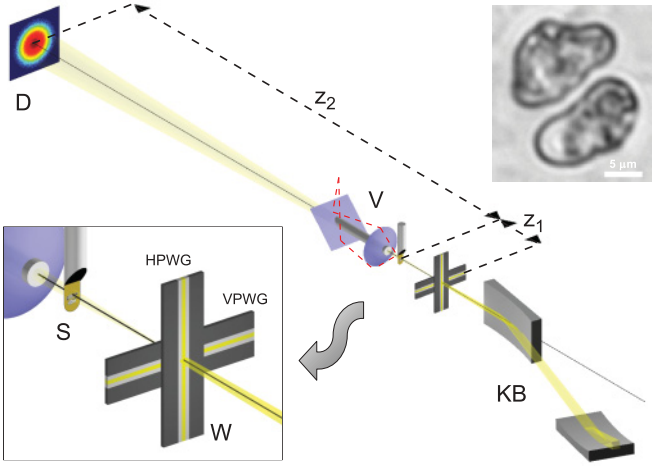

FIG. 1. (Color) Experimental setup. The x-ray beam is focused by two KB mirrors onto the system of two crossed planar WGs with a layered guiding core structure for optimized transmission. Two-dimesional-beam confinement is achieved by crossing a horizontally confining planar waveguide (HPWG) upstream with a second, vertically confining waveguide (VPWG) downstream. The sample holder (S) with freeze-dried *D. discoideum* cells attached to a thin polyimide film is placed at a distance z_1 from the WG system. The cells (for an optical micrograph, see inset on the upper right, scale bar 5 μm) can be visualized during the experiment using an optical video microscope (V) with a drilled lens to allow for the passage of the x-ray beam. An area detector is placed at a distance $z_2 \gg z_1$ away from the sample to collect the intensity diffracted from the sample.

(Christ, Germany) and used for imaging. Further details of the preparation process are described in [18].

The detector, a single-photon counting device [19] (Maxipix, ESRF) without readout noise and a pixel width of $\Delta_D = 55$ μm, was placed $z_2 = 3.09$ m away from the sample. The position of the sample is already well in the far field of the WG source, leading to a simplified description of the illuminating wave at the sample plane as a product of an ideal spherical wave and the Fourier transform of the WG exit wave field [20]. Within the paraxial approximation, the imaging experiment can then be described in a well-known equivalent parallel-beam geometry [9,17] with a demagnified detector pixel size of Δ_D/M and a (de)magnification factor of $M = (z_1 + z_2)/z_1$ as well as an effective sample-detector distance $z_{\text{eff}} = z_1 z_2/(z_1 + z_2) = z_2/M$. Note that here $z_2 \gg z_1$, so that $z_{\text{eff}} \simeq z_1 = 8.83$ mm and $M \simeq z_2/z_1 = 351$.

A total of 451 intensity distributions $I^{(n)}$ were collected with the sample in the beam at an exposure time of 0.2 s for each measurement, along with 451 empty images $I_0^{(n)}$ with equal exposure time. The images were collected in a sequence $(I^{(1)}, I_0^{(1)}, I^{(2)}, I_0^{(2)}, \ldots)$ with short time delays on the order of 1 s between exposures, facilitated by the fast piezo sample stage (PI, Germany) and the short readout time of the detector. Following this approach, fluctuations and long-term drift in the WG exit wave were eliminated successfully. The normalized intensity distribution shown in Fig. 2(a) was calculated as $\bar{I}(x,y) = \sum_n I^{(n)} / \sum_n I_0^{(n)}$. During a total illumination time of 90.2 s with and without a sample in the beam, respectively, a total fluence of ca. 2.8×10^6 ph/μm^2 and a dose of ca. 0.8×10^3 Gy were applied to the sample, based on calculations presented in [22].

Note that the fluence at the sample, the quantity which mainly determines the dose and obtainable resolution [22], increases quadratically with z_1^{-1} in the present setup and can thus easily be varied experimentally without the need to change the illumination time. The maximum total flux exiting the WG was on the order of 6×10^8 ph/s (depending on the ring current and coupling of the KB focus into the WG). This flux corresponds to only 5.2% of the KB flux impinging onto the WG entrance [13]. This can be explained by the high numerical aperture of the KB beam coupled into the WG system and the relatively low degree of spatial coherence in the KB focus. Note that assuming an idealized plane wave illumination, finite difference simulations yield a transmission of 90.4% for the present WG geometry and photon energy [13].

A correction of residual low frequency-variation in the normalized intensity distribution was performed independently for the vertical and horizontal direction through division by the mean intensity fluctuations in the regions outside the cellular

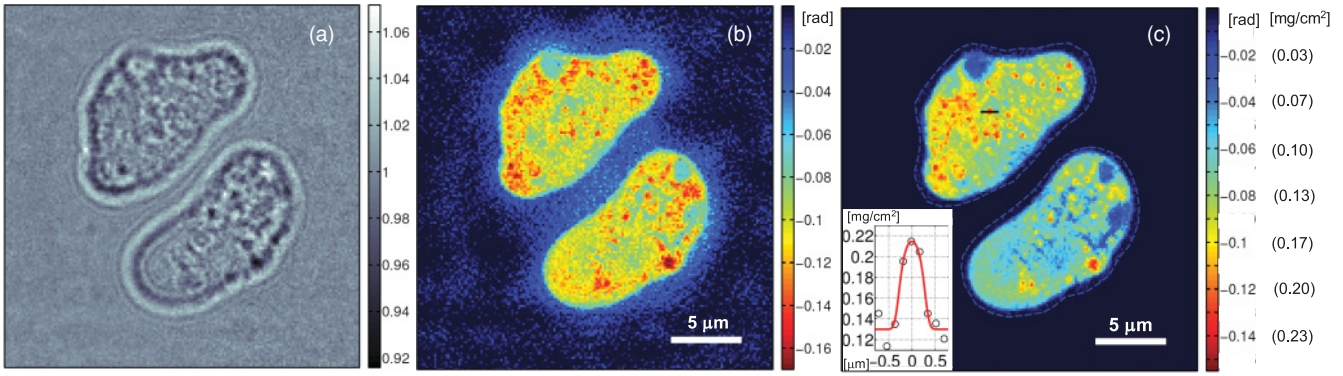

FIG. 2. (Color) Holographic intensity diffracted from freeze-dried *D. discoideum* cells, normalized by the empty WG intensity (a). Iterative reconstruction of the object phase, obtained after 200 GS iterations (b). Phase reconstruction obtained with a modified HIO scheme for pure phase objects as described in the main text (c). The boundary of the support area was determined from a holographic reconstruction and is marked here by a dashed blue line. The color bar is scaled in rad and also mg/cm^2, indicating the projected effective mass density of the cells [21]. A line scan through a globular region of higher density is indicated in the upper cell by a thin black line and reproduced in the inset on the lower left (open circles), along with a model curve (red solid line; see main text).

area, as determined from sums over empty columns and rows, respectively.

III. ANALYSIS

Following [22,23] with parameters adapted to the photon energy of the present experiment, the expected phase shift and amplitude attenuation of an unstained 3-μm-thick biological object with a protein volume content of 50% is $\Delta\phi = 0.13$ rad and $A = 1.04 \times 10^{-4}$, respectively, characterizing a cell as an essentially pure (and quite weak) phase object.

Diffraction effects within the sample are negligible, as long as the sample thickness Δz obeys [24]

$$\Delta z < \frac{r^2}{\lambda}, \tag{1}$$

where r denotes the lateral resolution of the experiment and λ the x-ray wavelength. Equation (1) denotes the maximum depth of focus of the experiment, that is, an upper limit of the projection approximation. Consequently, at a sample thickness of 5 μm diffraction effects do not have to be taken into account for lateral resolutions $r \gtrsim 27$ nm.

Obviously, condition (1) is easily met in the present case (see below for a discussion on the resolution), and the exit wave ψ_{out} in the plane directly behind the sample can be written as a product of the incident wave ψ_{in} and the sample transmission function χ. ψ_{in} is given here by the WG far field, which is approximately invariant under further free-space propagation, apart from geometric magnification. In the equivalent geometry described before, the recorded intensity at lateral position (x,y) is then given as $I(x,y) = |D_{z_{\text{eff}}}[\psi_{\text{in}}(x,y)\chi(x,y)]|^2 \simeq |\psi_{\text{in}}(x,y)|^2 |D_{z_{\text{eff}}}[\chi(x,y)]|^2$, where $D_{z_{\text{eff}}}$ denotes the two-dimensional Fresnel propagator over the distance z_{eff} along the optical axis. If the sample wave is written as $\chi(x,y) = 1 + \tau(x,y)$, one recovers the standard nomenclature of in-line holography, with the reference wave $R(x,y) = D_{z_{\text{eff}}}[\psi_{\text{in}}(x,y)] \simeq \psi_{\text{in}}(x,y)$, the object wave $O(x,y) = \psi_{\text{in}}(x,y) D_{z_{\text{eff}}}[\tau(x,y)]$, and the detected intensity $I = |R + O|^2$. The measured signal, normalized by the intensity $I_0(x,y) = |D_{z_{\text{eff}}}[\psi_{\text{in}}(x,y)]|^2 \simeq |\psi_{\text{in}}(x,y)|^2$ of to the empty beam, which is obtained in a separate measurement, is then given by

$$\begin{aligned} \bar{I}(x,y) &\simeq |\psi_{\text{in}}(x,y)|^2 |D_{z_{\text{eff}}}[\chi(x,y)]|^2 / |\psi_{\text{in}}(x,y)|^2 \\ &= |D_{z_{\text{eff}}}[\chi(x,y)]|^2. \end{aligned} \tag{2}$$

Backpropagation of Eq. (2) leads to a single-step holographic reconstruction of the normalized intensity $\bar{I}(x,y)$, which is, however, intrinsically spoiled by the so-called twin image.

A. Application of a Gerchberg-Saxton algorithm

A possible alternative to recover the object function $\chi(x,y)$ is given by iterative methods. Notably, in the present case of a pure phase object the object amplitude $|\chi(x,y)|$ is equal to unity in the object plane. The corresponding knowledge of the object wave amplitude in the sample *and* detector plane strongly simplifies the reconstruction problem and allows for the application of the well-known Gerchberg-Saxton (GS) algorithm [25]. A GS reconstruction of the experimental hologram, starting the iteration with a plane wave as an initial guess, is shown in Fig. 2(b). 200 iterations were used here, as a compromise between the general quality of the reconstruction, which improves with the iteration number, and the amount of noise introduced into the reconstruction from the noisy data. The reconstruction error was measured here by the misfit

$$d^2(|\tilde{\chi}_n|^2) := 1/N \sum_{(x,y)} [|\tilde{\chi}_n(x,y)|^2 - \bar{I}(x,y)]^2 \tag{3}$$

between the reconstructed and measured holographic intensity. Here $\tilde{\chi}(x,y) = D_{z_{\text{eff}}}[\chi(x,y)]$ denotes the near-field propagated object wave and N denotes the number of points (x,y), or pixels, at which $\bar{I}$ was measured.

B. A hybrid-input-output scheme applied to the phase

A significant improvement of the reconstruction was then achieved by application of a modified version of the classical hybrid-input-output (HIO) algorithm [26] for pure phase objects, which can be regarded as an extension of the scheme proposed in [27], where an update of the current amplitude $|\chi_n|$ was suggested according to

$$|\chi_{n+1}| = |\chi_n| - \beta(|\chi'_n| - 1), \tag{4}$$

slowly pushing $|\chi_n|$ toward 1. $|\chi'_n|$ denotes the amplitude of the nth iterate after application of the detection plane constraint, that is, $\chi'_n := P_M(\chi_n)$ with $P_M(\chi_n) = D_{-z_{\text{eff}}}[\sqrt{\bar{I}} \cdot \exp(i\varphi(\tilde{\chi}_n))]$ denoting the modulus replacement operation in the detection plane and $\varphi(z) := \arg(z)$ for any $z \in \mathbb{C}$. For the present analysis, a phase constraint was added to the update of the amplitude, namely,

$$\begin{aligned} &\varphi(\chi_{n+1}(x,y)) \\ &\quad = \begin{cases} \varphi(\chi_n(x,y)) - \gamma\varphi(\chi'_n(x,y)) \ \forall\ (x,y) \notin S \\ \min\{\varphi(\chi'_n(x,y)), 0\} \ \forall\ (x,y) \in S. \end{cases} \end{aligned} \tag{5}$$

The support area $S \subset \mathbb{R}^2$ can be determined here very accurately from a single-step holographic inversion of Eq. (2). Similar to the amplitude constraint (4) the phase constraint (5) causes a gentle decrease of the phase to a constant C ($C = 0$ was chosen here) in the area, where no object is located. The phase inside the support area, however, is left untouched, as long as it is not larger than C, allowing for phase changes $\Delta\varphi(x,y)$ in one direction only, as expected for objects with $|\Delta\varphi(x,y)| < \pi$. The speed of convergence is determined by the feedback parameters $\gamma \in [0,1]$ and $\beta \in [0,1]$.

The phase reconstruction shown in Fig. 2(c) was obtained by averaging the complex reconstructions from 25 independent runs of the modified HIO algorithm, which stopped at an average iteration number of $N_{\text{it}} = 2347$ and showed a very small distribution of the resulting phase values with a standard deviation below 3.5×10^{-4} rad in each pixel. As an initial guess a numerically generated realization of the random function

$$R = \begin{cases} 1 + a_0 Z_J \exp(i\phi_0 Z_J) & \text{if } (x,y) \notin S, \\ 1 + a_0 Z_J \exp[i(\phi_0 Z_J - 0.1)] & \text{else}, \end{cases} \tag{6}$$

assigned to each pixel at position (x,y), was used. The parameters a_0 and ψ_0 were chosen as $a_0 = \phi_0 = 0.2$ and equally distributed pseudorandom numbers on the interval

$J = [-0.5,0.5]$ were used for Z_J. The algorithmic feedback parameters were set to $\beta = \gamma = 0.2$ in the present example.

The maximum experimentally determined phase change of ca. 0.14 rad due to the freeze-dried cells is in agreement with expected values (see above). As described earlier [21] in the present case of a pure phase object the reconstructed phase distribution can be rescaled into a projected electron or, for light biological materials, mass density map [see additional color-bar scaling in Fig. 2(c)] with a density range well in agreement to what has been found before for unstained (bacterial) cells [21].

In the reconstruction shown in Fig. 2(c) several subcellular features are visible. While it cannot be excluded that some features such as the rather large void areas could be due to possible ruptures in the freeze-drying process, characteristic and abundant globular features of several hundred nanometers in size are attributed to mitochondria, providing chemical energy for the highly active and mobile state in which the cells were fixated. A simple spherical model [see Fig. 2(c)] with a mitochondrion mass density of 1.35 g/cm^3 is in coarse agreement with a reported value of 1.315 g/cm^3 for the dry density from rat liver mitochondria [28]. For the mitochondrion marked in Fig. 2(c) a sphere diameter of 0.64 μm was assumed and, to account for the finite experimental resolution, the resulting projected density profile was convoluted by a normal distribution with a FWHM equal to the pixel size of 157 nm.

C. Treatment of experimental noise

Experimental noise in the diffraction data can significantly disturb the results of iterative reconstruction schemes [29]. These are based on the implicit assumption that the measured intensity is a noise-free representation of the diffracted intensity, when the Fourier amplitude of the current iterate in Fourier space is replaced with the measured amplitude during each iteration. To prevent possible overfitting of the noise in the diffraction data a modified version of the modulus replacement operator P_M was used in [21] which projects the current iterate χ_n onto a sphere with finite radius $D > 0$ around the closest element of the modulus constraint set. The algorithm leaves the amplitude $|\tilde{\chi}_n|$ unchanged, as soon as χ_n falls within the sphere of radius D. An optimum value for D can be estimated from the noise statistics of the measured data.

In the present case a similar modified modulus operator was used, but now applied to the image intensity rather than the amplitude [21] with the intensity metric as defined in Eq. (3). The detection plane intensity of the updated χ_n' at position (x,y) thus reads

$$|\tilde{\chi}_n'(x,y)|^2 := \left(1 - \frac{D}{d}\right) \bar{I}(x,y) + \frac{D}{d} |\tilde{\chi}_n(x,y)|^2 \qquad (7)$$

if $d > D$. The algorithm was stopped as soon as $d \leqslant D$. The full modified detection plane operation is thus given as

$$\chi_n' = D_{-z_{\text{eff}}}[|\tilde{\chi}_n'| \exp(i\varphi(\tilde{\chi}_n))]. \qquad (8)$$

To find an optimum value for the parameter D one needs to consider the noise statistics of the experimental data. This enters the modulus replacement operator here as the normalized intensity distribution $\bar{I}(x,y)$, that is, the measured intensity $I(x,y)$ of the Fresnel-diffracted exit wave behind the sample, divided by the intensity of the empty beam $I_0(x,y)$. Both $I(x,y)$ and $I_0(x,y)$ are Poissonian random variables, but in order to discriminate the weak sample-signal from the empty beam, they both were measured at a high absolute count number (on the order of 10^5 counts per pixel) and can then be well-described as normally distributed quantities with means $\langle I(x,y)\rangle$, $\langle I_0(x,y)\rangle$, respectively, and approximately equal standard deviations $\sigma = \sqrt{\langle I_0(x,y)\rangle}$. Henceforth, the brackets $\langle\cdots\rangle$ without an index denote an average over the ensemble of all possible values (realizations) of $I(x,y)$ and $I_0(x,y)$.

According to error propagation of Gaussian random variables the normalized intensity

$$\bar{I}(x,y) := \frac{I(x,y)}{I_0(x,y)} \qquad (9)$$

then has a mean and variance of

$$\langle \bar{I} \rangle \approx \frac{\langle I \rangle}{\langle I_0 \rangle} \qquad (10)$$

$$\langle (\bar{I} - \langle \bar{I} \rangle)^2 \rangle \approx \tilde{\sigma}^2 = \frac{2}{\langle I_0 \rangle}, \qquad (11)$$

respectively, which are true for every position (x,y), at which $I(x,y)$ and $I_0(x,y)$ have been measured. Note that experimentally only realizations of $\bar{I}$ and $\bar{I}_0$ can be measured at each position and that the expectation values $\langle \bar{I} \rangle$ and $\langle \bar{I}_0 \rangle$ can only be obtained approximately in a measurement.

The (unknown) expectation value $\langle \bar{I} \rangle$ can be identified with the current guess $|\tilde{\chi}_n(x,y)|^2$ of the "true" intensity in Eq. (7); similarly the random variable $\bar{I}$ can be identified with the measured value $\bar{I}$. From Eqs. (3) and (11) and these identifications we can thus infer that

$$\begin{aligned} \langle d^2 \rangle &= \frac{1}{N} \sum_{(x,y)} \langle [\bar{I}(x,y) - |\tilde{\chi}_n(x,y)|^2]^2 \rangle \\ &= \frac{1}{N} \sum_{(x,y)} \frac{2}{\langle I_0 \rangle (x,y)}. \end{aligned} \qquad (12)$$

In an experiment we can only measure realizations of the summand $2/I_0(x,y)$ and then obtain the noisy sum

$$\frac{1}{N} \sum_{(x,y)} \frac{2}{I_0(x,y)} \to \frac{1}{N} \sum_{(x,y)} \frac{2}{\langle I_0 \rangle (x,y)} = \frac{2}{\langle I_0 \rangle}, \qquad (13)$$

which, however, converges against the result on the right for long measurement times and under the assumption that $\langle I_0 \rangle (x,y)$ is constant; that is, the detector is illuminated uniformly by the WG beam. A natural choice for the threshold parameter D is thus $D_{\text{th}} = \sqrt{2/\langle I_0 \rangle}$, providing a criterion when to stop the algorithm.

For feedback parameters $\beta = \gamma = 0.2$, the smallest D for which convergence (in the sense of reaching a stop criterion) could be achieved within a reasonable amount of time (<5000 iterations) was found to be $D = 1.06 D_{\text{th}}$. The minute deviation from one can be caused by the not strictly uniform illumination function, which has been assumed in the derivation of D_{th}. $D = 1.06 D_{\text{th}}$ was then used for all reconstructions, including those obtained from simulated data, in order to make the results better comparable.

D. Reconstruction errors

To study reconstruction errors in the obtained phase map of the freeze-dried cells a phantom object was generated with similar size and scattering power as the cells, that is, a maximum phase shift and amplitude attenuation of $\Delta\varphi = 0.13$ rad and $A = 1.04 \times 10^{-4}$, respectively. The phantom object was subject to the same total fluence and the same experimental parameters (z_1, z_2, etc.) as used in the real experiment. The reconstruction was performed with the same set of algorithmic parameters (β, γ, etc.) as used for the experimental data. The simulated phantom phase is depicted in Fig. 3(a), while the reconstructed phase map is shown in Fig. 3(b), indicating strong agreement between simulation and reconstruction. Note that the original phase map is shown here with the full simulated resolution, that is, a pixel size of 39 nm. From this phase map a hologram was simulated and subsequently interpolated to the experimental pixel size. The reconstruction is shown with the same pixel size as the experimental reconstruction shown in Fig. 2(c). The root mean square (rms) deviation between the simulated and reconstructed phantom phase within the support area was 0.012 rad with a largest absolute phase deviation of 0.038 rad. These values are significantly above the standard deviation of the reconstructed phase in each pixel, taken over the ensemble of 25 reconstructed object transmission functions, from which the final result was generated as the mean.

For weak objects the free-space Fresnel-propagator D_z can be regarded as a spatial filter with zero-frequency response to the incident phase map at spatial frequencies $\nu_n = \sqrt{n/\lambda z}$ ($n \in \mathbb{N}_0$) [17]. The associated phase-contrast transfer function [PCTF; cf. Fig. 3(d)] is thus characterized by zeros at these

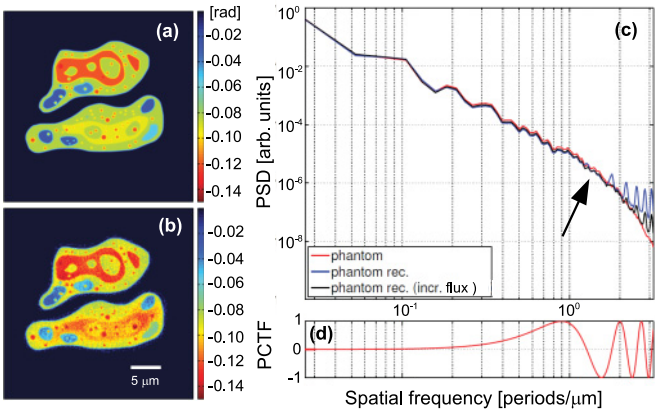

FIG. 3. (Color) Phase map (a) of a simulated object transmission function for an unstained biological cell with parameters as used in the real experiment and (b) iterative reconstruction obtained with the modified HIO scheme described in the main text. The angular averaged power spectral density (PSD) of the simulated phase map is shown as a red line in panel (c). For comparison, the PSD of the reconstruction from the simulated data is plotted (blue line) along with a PSD of a reconstruction from modeled data with 10 times more simulated flux (black line). The HIO scheme successfully recovers the spatial frequency component marked by an arrow, where there is a zero in the phase-contrast transfer function (PCTF) (d). Notably, an increase in simulated flux results in the recovery of more unconstrained frequencies.

spatial frequencies, which are not encoded in the diffraction pattern $|\tilde{\chi}(x,y)|^2$, given a complex object wave $\chi(x,y)$.

One way to recover these frequencies is the simultaneous iterative reconstruction from diffraction patterns obtained at various distances z, as demonstrated very successfully before [2,3]. However, one might be forced to keep the incident dose as small as possible, especially in high-resolution tomographic mode, to prevent radiation damage, or measurements at different propagation distances might not even be possible, such as in applications at free-electron lasers, where the sample is severely damaged after exposure to a single incident pulse train. In such situations one has to recover phase information from a single "holographic" image. From the comparison of a simulated phase distribution of a biological cell and its power spectral density (PSD) on the one side, with the iterative reconstruction of the simulated data and the corresponding PSD (see Fig. 3) on the other side, it becomes evident that the lost frequencies can be recovered to a very large extent, using the modified HIO reconstruction scheme described above. Only residual local maxima are present at unconstrained frequencies in the reconstructed PSD. We attribute this effect to the analyticity of the Fourier transform of a complex two-dimensional function with a compact support. In such a case an analytic continuation of the Fourier transform is possible given its knowledge on a finite area, a phenomenon which can lead to so-called "bandwidth-extrapolation" [30]. It helps here to fill out missing information due to zeros in the PCTF. Importantly, by increasing the number of incident photons (here by a factor of ten), the unconstrained frequency components are recovered even better [see black line in Fig. 3(a)].

We also explored the effect of an increased fluence on the sample just by increasing the geometrical magnification and leaving the total photon number the same as in the present experiment. To demonstrate an associated increase in spatial resolution (see below), the phantom chosen here was a Siemens star with amplitude transmission of 1 and a maximum phase change of $\Delta\varphi = 0.13$ rad. In Fig. 4 the PSDs corresponding to the simulated Siemens star test pattern [see Fig. 5(a)], its holographic reconstruction and its iterative HIO-based reconstruction are shown. While the PSD of the holographic reconstruction has characteristic minima at frequencies of zero-contrast transfer, such artifacts are almost completely removed in the iterative reconstruction based on the modified HIO scheme.

E. Spatial resolution

If sample scattering is weak and no scattered photons are detected outside the WG exit wave field, the spatial resolution is determined by the wave field opening angle, limiting the resolution roughly to the beam diameter at the WG exit plane [20]. In the present experiment, however, the resolution was rather limited by the relatively large defocus distance z_1 dictated by steric constraints of the positioning devices. The resulting (half-period) resolution on the order of one to two pixels (with an effective pixel size of 157 nm) thus has to be assessed in view of the very low dose of ca. 0.8×10^3 Gy and confirms previous results with similar parameters [21]. In addition, the modest resolution is associated in the present

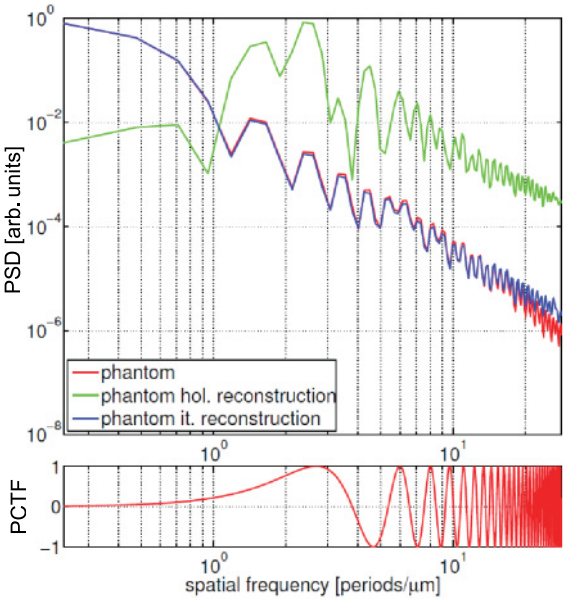

FIG. 4. (Color) The power spectral density (PSD) of a simulated object transmission function for a weakly scattering Siemens star test pattern is shown in comparison to the PSD of the holographic and the iterative reconstruction from the simulated data, based on the modified HIO scheme (a). See Fig. 5 for the corresponding real-space images. Although the zeros of the contrast transfer function have a strong influence on the holographic reconstruction, in this case the iterative reconstruction is essentially free of such artifacts, and the object transmission function is recovered for nearly all spatial frequencies. The phase-contrast transfer function corresponding to the simulated experimental geometry is shown in panel (b).

case with a relatively large field of view of ca. $38 \times 38\ \mu$m from a single measured diffraction pattern.

To demonstrate the resolution range that can in principle be achieved with the present WG and detector parameters, aside from the instrumentation constraints, we have performed simulations on a Siemens star phantom object [see Fig. 5(a)] with phase shifts alternating between $\varphi \simeq -0.10$ and $\varphi \simeq -0.13$ rad in the light and dark stripes, respectively. The geometric magnification was adjusted to 9 times the magnification of the real experiment, by decreasing z_1 to ca. 1 mm, leading to a pixel size of 17.5 nm. The total number of photons, 4×10^9, in the simulated WG exit field was set *equal* to that of the experiment. The WG exit wave field was modeled as a Gaussian with an intensity FWHM of 10 nm, resulting in an average fluence of 2.2×10^8 ph/μm^2 at the sample. A

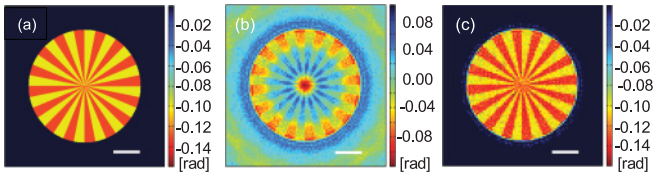

FIG. 5. (Color) Original phase map from a simulated Siemens star test pattern with a phase difference of 0.03 rad between the light and dark stripes (a), together with the holographic (b) and iterative reconstruction (c), using a modified HIO scheme. Scale bars indicate 250 nm.

comparison of the simulated and the iteratively reconstructed phase map is shown in Fig. 5, indicating a quantitative reconstruction. The rms deviation between the reconstruction and the phantom phase within the area of the Siemens star was found to be 0.008 rad. While the holographic reconstruction is severely distorted at frequencies corresponding to zeros in the PCTF, the iterative reconstruction, applied here with the same algorithmic parameters as used for the experimental data, is free of such artifacts. A comparison of the power spectral densities of the original object phase and the reconstruction indicates a (half-period) resolution close to the pixel size of the hologram, 17.5 nm [see Fig. 4].

F. Coherence requirements

The coherence requirements for propagation-based diffractive imaging using x-ray WGs as quasi-point-sources have been discussed in detail before [31] and we shortly review the main considerations in the context of the present experiment.

A particular advantage of the present setup is the essentially full spatial coherence of the beam incident on the sample, provided by the very small source diameter of the WG exit wave field [13]. On the other hand, the bandpass $\Delta\lambda/\lambda \simeq 0.02$ of the pink-beam undulator radiation that is coupled into the WG leads to a rather limited longitudinal coherence length. However, the propagation-based imaging process will not be affected by this spread in wavelength, as long as

$$\frac{\Delta\lambda}{\lambda} \leqslant \frac{1}{\lambda z_{\mathrm{eff}} \nu^2}, \tag{14}$$

considering the problem in one dimension here for clarity. Given an effective pixel size of Δ, the largest possible (full-period) spatial frequency that can be resolved is $1/(2\Delta)$ (the Nyquist frequency), so that the maximum allowable bandpass becomes

$$\frac{\Delta\lambda}{\lambda} \leqslant \frac{4\Delta^2}{\lambda z_{\mathrm{eff}}}. \tag{15}$$

With $4\Delta^2/(\lambda z_{\mathrm{eff}}) \simeq 0.16$ this is still fulfilled in the present experimental situation. However, for higher resolution a lower bandpass is desirable which can be achieved by using a crystal monochromator. For the novel dedicated setup [32] installed at the beamline P10 of the PETRA III storage ring at DESY in Hamburg, Germany, the intensity loss due to the monochromator will be tolerable due to the extremely high brilliance of the synchrotron source.

IV. CONCLUSION

In summary, we have demonstrated WG-based x-ray microscopy of unstained biological cells. The method takes advantage of a new generation of crossed high-transmission planar WGs allowing for beam confinement below 15 nm and, together with optimized iterative reconstruction schemes, allows for stable and fast reconstructions of the sample transmission function, with small and quantifiable errors. The possible resolution range has not been fully exploited yet, but simulations with realistic parameters indicate that resolutions

in the range of the WG beam confinement are possible, even for relatively weak contrast values. The reconstruction scheme, using only one holographic image without detailed knowledge of the illumination, is widely applicable in propagation-based hard-x-ray imaging of biological objects and underlines the simplicity and dose-efficiency of the method. It also opens up possible applications at new x-ray free-electron laser sources presently commissioned or constructed.

ACKNOWLEDGMENTS

We thank R. Tucoulou and P. Cloetens for excellent support at the ID22 beamline and E. Bodenschatz for discussion and continuous support. R. N. Wilke is thanked for discussions. Funding by the DFG collaborative research center SFB 755, the Helmholtz Society (VI-203), and the German Ministry of Education and Research (Grant No. 05KS7MGA) is gratefully acknowledged.

[1] K. A. Nugent, Adv. Phys. **59**, 1 (2010).
[2] P. Cloetens *et al.*, Appl. Phys. Lett. **75**, 2912 (1999).
[3] P. Cloetens *et al.*, Proc. Natl. Acad. Sci. USA **103**, 14626 (2006).
[4] S. W. Wilkins *et al.*, Nature (London) **384**, 335 (1996).
[5] V. E. Cosslett and W. C. Nixon, J. Appl. Phys. **24**, 616 (1953).
[6] D. Gabor, Nature (London) **161**, 777 (1948).
[7] S. Eisebitt *et al.*, Nature (London) **432**, 885 (2004).
[8] G. J. Williams, H. M. Quiney, B. B. Dhal, C. Q. Tran, K. A. Nugent, A. G. Peele, D. Paterson, and M. D. de Jonge, Phys. Rev. Lett. **97**, 025506 (2006).
[9] C. Fuhse, C. Ollinger, and T. Salditt, Phys. Rev. Lett. **97**, 254801 (2006).
[10] L. De Caro, C. Giannini, D. Pelliccia, C. Mocuta, T. H. Metzger, A. Guagliardi, A. Cedola, I. Burkeeva, and S. Lagomarsino, Phys. Rev. B **77**, 081408(R) (2008).
[11] T. Salditt, S. P. Kruger, C. Fuhse, and C. Bahtz, Phys. Rev. Lett. **100**, 184801 (2008).
[12] K. Giewekemeyer *et al.*, New J. Phys. **12**, 035008 (2010).
[13] S. P. Krüger *et al.*, Opt. Express **18**, 13492 (2010).
[14] D. Shapiro *et al.*, Proc. Natl. Acad. Sci. USA **102**, 15343 (2005).
[15] C. Song, H. Jiang, A. Mancuso, B. Amirbekian, L. Peng, R. Sun, S. S. Shah, Z. H. Zhou, T. Ishikawa, and J. Miao, Phys. Rev. Lett. **101**, 158101 (2008).
[16] Y. Nishino, Y. Takahashi, N. Imamoto, T. Ishikawa, and K. Maeshima, Phys. Rev. Lett. **102**, 018101 (2009).
[17] S. Mayo *et al.*, J. Microsc. **207**, 79 (2002).
[18] K. Giewekemeyer, M. Hantke, C. Beta, R. Tucoulou, and T. Salditt, J. Phys. Conf. Ser. **186**, 012086 (2009).
[19] C. Ponchut *et al.*, Nucl. Instrum. Methods A **576**, 109 (2007).
[20] C. Fuhse, Ph.D. thesis, Georg-August-Universität Göttingen, 2006.
[21] K. Giewekemeyer *et al.*, Proc. Natl. Acad. Sci. USA **107**, 529 (2010).
[22] M. Howells *et al.*, J. Electron Spectrosc. **170**, 4 (2009).
[23] P. Thibault *et al.*, Acta Crystallogr. A **62**, 248 (2006).
[24] L. De Caro, C. Giannini, A. Cedola, S. Lagomarsino, and I. Bukreeva, Opt. Commun. **265**, 18 (2006).
[25] R. W. Gerchberg and W. O. Saxton, Optik (Jena) **35**, 237 (1972).
[26] J. R. Fienup, Appl. Opt. **21**, 2758 (1982).
[27] T. E. Gureyev, Opt. Commun. **220**, 49 (2003).
[28] C. De Luve, *Nobel Lectures, Physiology or Medicine 1971–1980* (World Scientific, Singapore, 1992).
[29] G. Williams *et al.*, Acta Crystallogr. A **63**, 36 (2007).
[30] J. W. Goodman, *Introduction to Fourier Optics* (Roberts & Company, Englewood, Colorado, 2005).
[31] T. Salditt, K. Giewekemeyer, C. Fuhse, S. P. Krüger, R. Tucoulou, and P. Cloetens, Phys. Rev. B **79**, 184112 (2009).
[32] S. Kalbfleisch *et al.*, AIP Conf. Proc. **1234**, 433 (2010).